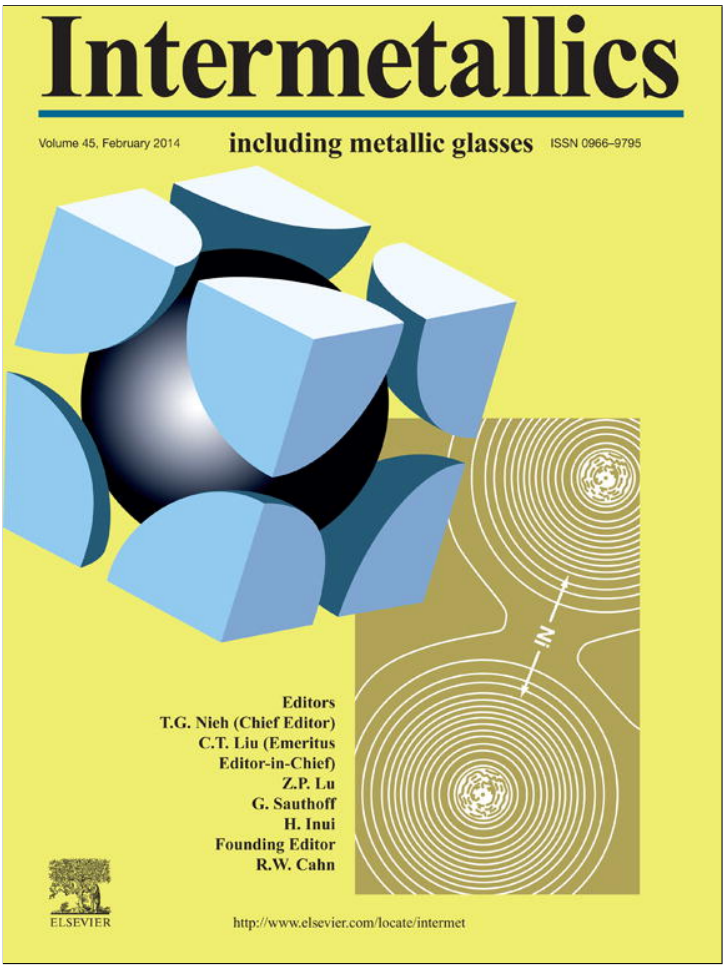

Intermetallics 45 (2014) 5–10

Contents lists available at ScienceDirect

Intermetallics

journal homepage: www.elsevier.com/locate/intermet

Drastic changes of electronic structure, bonding properties and crystal symmetry in Zr_2Cu by hydrogenation, from *ab initio*

Adel F. Al Alam [a], Samir F. Matar [b,c,*], Ahmad Jammal [d], Naïm Ouaini [a]

[a] Holy Spirit University of Kaslik, USEK, Jounieh, Lebanon
[b] CNRS, ICMCB, UPR 9048, F-33600 Pessac, France
[c] Univ. Bordeaux, ICMCB, UPR 9048, F-33600 Pessac, France
[d] Ministry of Higher Education, Beirut, Lebanon

ARTICLE INFO

Article history:
Received 22 July 2013
Received in revised form
13 September 2013
Accepted 16 September 2013
Available online 8 October 2013

Keywords:
A. Intermetallics, miscellaneous
B. Bonding
C. Interstitial content, control
E. Electronic structure, calculation

ABSTRACT

Gradual hydrogen uptake into Zr_2Cu intermetallic leads to crystal symmetry changes from tetragonal Zr_2CuH_2 to monoclinic Zr_2CuH_5. This experimental finding is explained here from cohesive energies computed within quantum DFT for Zr_2CuH_x ($x = 1, 2, 3, 4, 5$) models in both structures. The threshold is found at $2 < x < 3$ in agreement with experiment. Beside structural crossover, electronic properties, chemical bonding, and mechanical behavior are also analyzed. Metal–H interactions arising from increasingly H presence in Zr_2Cu lead to more and most cohesive and harder Zr_2CuH_2 and Zr_2CuH_5 respectively.

1. Introduction

Several binary intermetallic compounds based on zirconium are known as C15 *Laves* phases ZrT_2 [1] and Zr_2T [2], *T* being a transition metal. Besides mechanical properties in equiatomic Zr*T* such as the hardness sought for uses in biomedical materials [3] and shape memory applications [4], a major characteristic is in their ability of absorbing large amounts of hydrogen such as $ZrFe_2H_{3.5}$ [5], $ZrNiH_3$ [6] and Zr_2CuH_5 [7] which led to their investigation as potential candidates for hydrogen storage [8–10]. In this context, intermetallic Zr_2Cu belongs to the A_2Cu family (A = Ti, Zr, Hf) crystallizing in the body centered tetragonal $MoSi_2$-type (cf. Table 1) [8]. They can absorb hydrogen by occupying the [A_4] tetrahedral sites. The structure of Zr_2CuH_2 and tetrahedral H surroundings are shown in Fig. 1. Zr_2Cu hydrides can be of interest experimentally because they decompose slowly around 200 °C compared to 527 °C for similar Zr_2Pd [8]. This lets suggest significant iono-covalent character of hydrogen and lower enthalpies of formation.

The question arises as to whether more hydrogen can be absorbed while keeping the $MoSi_2$-type structure. In fact the hydrogen saturated compound Zr_2CuH_5 is found in a monoclinic structure shown in Fig. 1 with the different hydrogen environment [7]. The ordering of hydrogen often leads to structural distortion, e.g. body centered tetragonal Zr_2Co becomes primitive tetragonal with hydrogen ordering in Zr_2CoH_5 (cf. Ref. [11] and therein cited works). This is also observed in the cubic Laves phases C15 with *Fm*-3*m* space group (SG), which becomes monoclinic in *P*1*n*1 SG in saturated YFe_2H_5 [9].

It becomes subsequently relevant to examine the composition threshold at which the monoclinic phase stabilizes in Zr_2CuH_x based on energy criteria. These aspects and the effects of increasing amounts of hydrogen on the mechanical properties and the iono-covalent behavior of hydrogen can be addressed quantitatively in the framework of the quantum density functional theory (DFT) [12]. This is the aim of the present work.

2. Structural details

The structures of tetragonal Zr_2Cu and Zr_2CuH_2, and monoclinic Zr_2CuH_5 are described in Table 1 and sketched in Fig. 1. The di-hydrogenated ternary has the tetragonal $MoSi_2$-type structure (*I*4/*mmm* space group SG). Fig. 1(a) shows H located in edge sharing [Zr_4] tetrahedra at (4*d*) Wyckoff position [7]. The saturated monoclinic structure has five coordination polyhedra for H as shown in Fig. 1(b): (i) tetrahedral [Zr_4] and [Zr_3Cu] coordinations, and (ii)

* Corresponding author. CNRS, ICMCB, UPR 9048, F-33600 Pessac, France. Tel.: +33 540002690; fax: +33 54002761.
E-mail addresses: matar@icmcb-bordeaux.cnrs.fr, abouliess@gmail.com (S.F. Matar).

0966-9795/$ – see front matter © 2013 Elsevier Ltd. All rights reserved.
http://dx.doi.org/10.1016/j.intermet.2013.09.009

Table 1
Experimental and (calculated) crystal data for Zr_2Cu, Zr_2CuH_2 and Zr_2CuH_5 [7,8]. SG: space group. FU = formula unit.

Zr_2Cu			
SG#139 *I*4/*mmm*			
$MoSi_2$, C11*b*-type			
a = 3.120 (3.21) Å			
c = 11.183 (11.23) Å			
V = 108.86 (115.7101) Å^3			
At.(Wyck.)	x	y	z
Cu (2*a*)	0	0	0
Zr (4*e*)	0	0	0.340 (0.345)
Total energy (eV)/FU: −21.08 eV			
Zr_2CuH_2			
SG#139 *I*4/*mmm*			
$MoSi_2$, C11*b*-type			
a = (3.256) Å			
c = (11.796) Å			
V = (125.06) Å^3			
Hypo. 1			
At. (Wyck.)	x	y	z
Cu (2*a*)	0	0	0
Zr (4*e*)	0	0	(0.361)
H (4*d*)	0	½	¼
d(Zr–H) = 2.09 Å			
Total energy (eV)/FU: −29.13 eV			
Hypo. 2: H (4*e*) 0 0 z ($z_{calc.}$ ~ 0.17): d(Zr–H) = 2.20 Å; $E_{TOT.}$ = −28.87 eV.			
Hypo. 3: H (4*c*) 0 ½ 0 : d(Cu–H) = 1.73 Å; $E_{TOT.}$ = −28.04 eV.			
Zr_2CuH_5			
SG#12 *I*2/*m*			
Exp. Ref. [7]			
a = 9.336 (9.882) Å			
b = 3.603 (3.667) Å			
c = 8.343 (8.390) Å			
β = 104.29° (103.93°)			
V = 271.94 (278.06) Å^3.			
At.(Wyck.)	x	y	z
Cu (4*i*)	0.3792 (0.377)	0	0.5250 (0.529)
Zr1 (4*i*)	0.0768 (0.081)	0	0.2320 (0.236)
Zr2 (4*i*)	0.6653 (0.683)	0	0.086 (0.100)
H1 (4*i*) (Zr_4)	0.1385 (0.134)	0	0.7211 (0.711)
H2 (4*i*) (Zr_4)	0.4617 (0.464)	0	0.1419 (0.140)
H3 (4*i*) (Zr_3Cu)	0.3155 (0.316)	0	0.2938 (0.296)
H4 (4*i*) (Zr_3Cu)	0.1883 (0.183)	0	0.4039 (0.482)
H5[a] (4*i*) (Zr_3Cu_2)	0.8895 (0.882)	0	0.0291 (0.022)
Shortest distances with H:			
• Zr substructure: d(Zr–H1) = 2.07 Å; d(Zr–H2) = 2.06 Å; d(Zr–H3) = 2.13 Å; d(Zr–H4) = 2.02 Å; d(Zr–H5) = 2.20 Å.			
• Cu substructure: d(Cu–H3) = 1.86 Å; d(Cu–H4) = 1.75 Å; d(Cu–H5) = 1.84 Å.			
Total energy (eV)/FU: −40.46 eV.			

[a] Experimental occupancy 0.71.

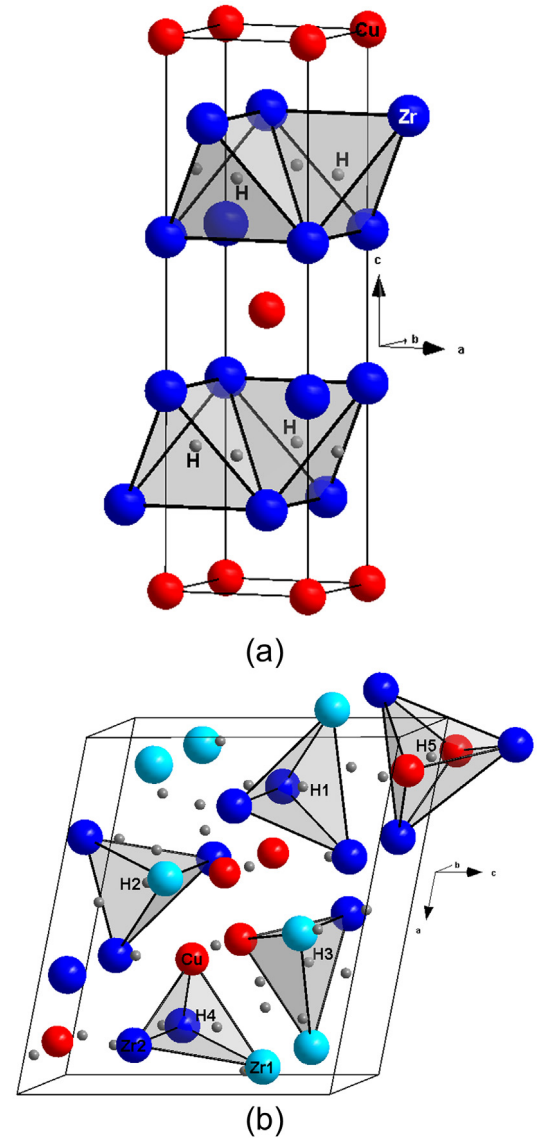

Fig. 1. Sketches of the crystal structure of: (a) tetragonal Zr_2CuH_2 with H in [Zr_4] tetrahedral site, and (b) the hydrogen rich monoclinic Zr_2CuH_5 showing the different environments of hydrogen atoms as given in Table 1.

prismatic [Zr_3Cu_2] coordination. The latter sites are partially populated by H. It is important to mention the similarity of the [Zr_4] coordination of H in both tetragonal and monoclinic structures, which lets suggest that the departure from such coordination in tetragonal structure should lead to destabilizing the ternary system. This is addressed in the upcoming sections.

Note that the determination of hydrogen positions from powder neuron diffraction data in the title compounds and in other compounds such as the intermediate hydrides of $MgPd_3$ [13] can be verified and predicted from computations as in the investigation of hydrogenated $LaNi_5$ and $LaCo_5$ [14].

3. Computation methods

Two computational methods within the DFT were used in a complementary manner. The Vienna ab initio simulation package (VASP) code [15] allows geometry optimization and total energy calculations. For this we use the projector augmented wave (PAW) method [16], built within the generalized gradient approximation (GGA) scheme following Perdew, Burke and Ernzerhof (PBE) [17]. Also preliminary calculations with local density approximation LDA [18] led expectedly to an underestimated volume versus the experiment. The conjugate-gradient algorithm [19] is used in this computational scheme to relax the atoms. The tetrahedron method with Blöchl corrections [16] as well as a Methfessel–Paxton [20] scheme were applied for both geometry relaxation and total energy calculations. Brillouin-zone (BZ) integrals were approximated using the special k-point sampling. The optimization of the structural parameters was performed until the forces on the atoms were less than 0.02 eV/Å and all stress components less than 0.003 eV/Å^3. The calculations are converged at an energy cut-off of 300 eV for the plane-wave basis set with respect to the k-point integration with a starting mesh of 4 × 4 × 4 up to 8 × 8 × 8 for best convergence and relaxation to zero strains. Using larger energy cut-off values as 500 eV did not lead to better convergence or to

different results (volume/energy). The calculations are scalar-relativistic.

Then all-electron calculations with the GGA were carried out for a full description of the electronic structure and the properties of chemical bonding, using full potential scalar-relativistic augmented spherical wave (ASW) method [21,22]. In the minimal ASW basis set, we chose the outermost shells to represent the valence states and the matrix elements were constructed using partial waves up to $l_{max}+1=3$ for Zr and Cu and $l_{max}+1=1$ for H. Self-consistency was achieved when charge transfers and energy changes between two successive cycles were below $10^{-8}\times e$ and 10^{-6} eV, respectively. BZ integrations were performed using the linear tetrahedron method within the irreducible wedge. In order to optimize the basis set, additional augmented spherical waves are placed at carefully selected interstitial sites (IS). Besides the site projected density of states, we discuss qualitatively the pair interactions based on the overlap population analysis with the crystal orbital overlap population (COOP) [23]. In the plots, positive, negative, and zero COOP indicate bonding, anti-bonding, and non-bonding interactions, respectively.

4. Results from PAW-GGA calculations

4.1. Geometry optimization and cohesive energies

The experimental and calculated structure parameters [7,8] are given in Table 1. The latter results show fairly good agreement with experiment for Zr_2Cu and Zr_2CuH_5. Larger volume magnitudes can be assigned to the use of GGA DFT functional which is underbinding compared to LDA and leads to overestimated lattice spacing. For the dihydride calculations were done using three hypotheses for two-fold hydrogen positions in the $MoSi_2$-type. The energy results clearly show preference for H in $[Zr_4]$ tetrahedra (Fig. 1(a)). When H is positioned in (4*e*) sites it is found in $[Zr_5]$ square planar prisms (Hypo. 2, Table 1) and the energy is higher. Finally when (4*c*) position is occupied by H (Hypo. 3, Table 1) the least favorable energy is obtained where H is in the vicinity of Cu with d(Cu–H) = 1.73 Å. This is significantly shorter than the Zr–H distances of 2.09 and 2.20 Å found when H is in the neighborhood of Zr in hypotheses 1 and 2. The difference of distance magnitudes likely arises from the difference of eletronegativity between Zr and Cu following the Pauling scale: $\chi_{Zr}=1.33$ and $\chi_{Cu}=1.90$. Although the metal–H is of iono-covalent character, the more electronegative copper leads to more covalent like Cu–H bonds versus more ionic like Zr–H which allows for larger charge transfer from Zr to H. This is also shown for the shortest distances of H with Zr and Cu substructures in Zr_2CuH_5 with systematically shorter Cu–H than Zr–H, reflecting the coordination polyhedra shown in Fig. 1(b), *i.e.* with no Cu–H1 or Cu–H2 contacts identified.

The magnitude of charges on the different constituents are also analyzed using the AIM (atoms in molecules theory) approach [24] developed by Bader who devised an intuitive way of splitting molecules into atoms as based purely on the electronic charge density. Typically in chemical systems, the charge density reaches a minimum between atoms and this is a natural region to separate them from each other. Such an analysis can be useful when trends between similar compounds are examined; they do not constitute a tool for evaluating absolute ionizations. Bader's analysis is done using a fast algorithm operating on a charge density grid [25]. The results of computed charges (Q) are such that they lead to neutrality when the respective multiplicities are accounted for. The obtained values for Zr_2CuH_2 in the three hypotheses are:

Hypo. 1: $Q(Zr)=+1.39e$; $Q(Cu)=-1.29e$; $Q(H)=-0.74e$.

Hypo. 2: $Q(Zr)=+1.10e$; $Q(Cu)=-0.77e$; $Q(H)=-0.71e$.

Hypo. 3: $Q(Zr)=+0.65e$; $Q(Cu)=-0.37e$; $Q(H)=-0.47e$.

Consequently regardless of the structure, H enters the intermetallic lattice in the neighborhood of zirconium which allows for the largest charge transfer, whence the larger stabilization. From Table 1 showing the crystal data of the monoclinic structure, this is also observed and the first two H are located in $[Zr_4]$ tetrahedra. $[Zr_3Cu]$ tetrahedra start being occupied at the third and fourth inserted hydrogen. Lastly the 5th H is located in prismatic $[Zr_3Cu_2]$ partially occupied.

In this context it is relevant to determine the composition threshold at which the monoclinic structure prevails over the tetragonal one from energy calculations. In the monoclinic ordering the calculations are done considering progressive filling of the hydrogen positions as shown in Table 1. For the tetragonal structure hypotheses 1 and 2 were followed in inserting H. The resulting total energies are plotted against hydrogen composition x_H in Fig. 2(a). The obtained energies are shown to decrease with the H composition in a closely linear manner. The linear fit parameters shown in the inserts indicate that at $x_H=0$, *i.e.* for the binary intermetallic, the tetragonal form is more stable than the monoclinic one in agreement with experimental findings [7,8]. Then as H enters the lattice, energy decreases further down showing a larger slope for the monoclinic structure. This implies that a crossover should occur. The tetragonal structure is more stable than the monoclinic one for the

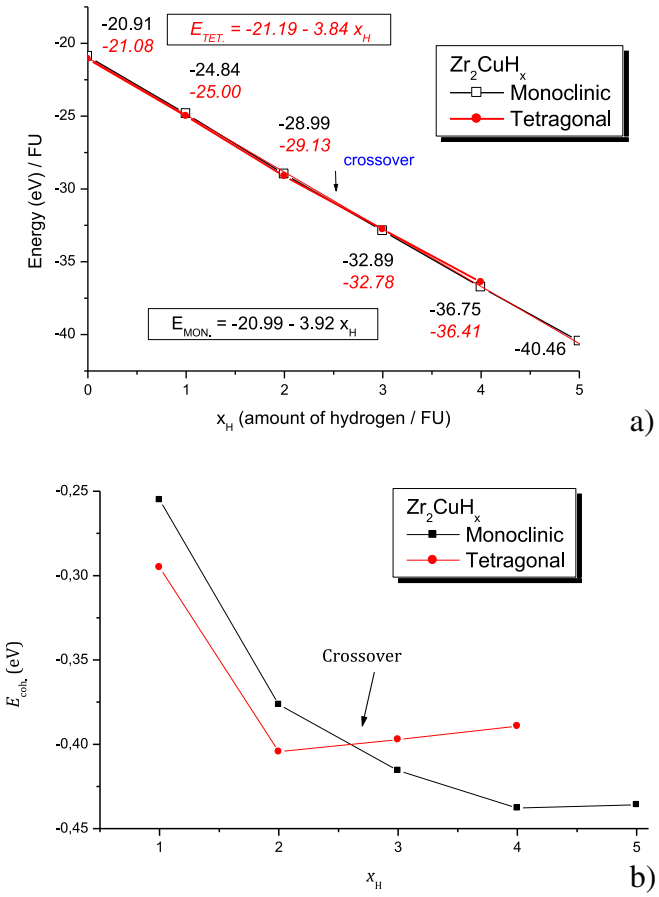

Fig. 2. (a) Total electronic energy versus hydrogen composition x_H, for Zr_2CuH_x models in tetragonal and monoclinic structures. Linear parameterizations fits provide steeper larger slope for the monoclinic structure. (b) Cohesive energies versus composition showing the same crossover region in Zr_2CuH_x models.

first two hydrogen atoms then there is a crossover between 2 and 3 H where the monoclinic form stabilizes for larger compositions. This shows that the tetragonal structure can only accommodate hydrogen in [Zr_4] tetrahedra then a distortion occurs towards a monoclinic structure which has more tetrahedral sites (Table 1). The linear decrease of the energy might be expected in as far as more and more hydrogen is loaded. But it could hide the non-linear behavior, which eventually drives the phase transition. Furthermore, more meaningful than the calculated energies are the cohesive energies. Therefore, a completed analysis of the results is provided in Fig. 2(b) showing the corresponding plot of the cohesive energies versus composition. The linear behavior is removed and one can observe that the crossover region is found similar as in Fig. 2(a). From the crystallography standpoint, the lowering of the symmetry leads to: (i) two Zr substructures instead of one, and (ii) the availability of further interstitial sites (monoclinic structure), whence the larger number of hydrogen. Also no stable solution could be found for $x_H = 5$ in the tetragonal structure. Following the monoclinic evolution, we obtained the cohesive energies from energy differences between the total energy of the compound and those of the atomic constituents Zr and Cu as well as dihydrogen which have the following energies from PAW-GGA calculations: $E(\mathrm{Cu}) = -3.715$ eV/atom, $E(\mathrm{Zr}) = -8.408$ eV/atom and $E(\mathrm{H_2}) = -6.577$ eV/$\mathrm{H_2}$. From the total electronic energies given in Fig. 2, the resulting cohesive energies are: $E_{\mathrm{coh.}}(\mathrm{Zr_2CuH_5}) = -0.436$ eV/atom; $E_{\mathrm{coh.}}(\mathrm{Zr_2CuH_4}) = -0.438$ eV/atom; $E_{\mathrm{coh.}}(\mathrm{Zr_2CuH_3}) = -0.415$ eV/atom; $E_{\mathrm{coh.}}(\mathrm{Zr_2CuH_2}) = -0.376$ eV/atom and $E_{\mathrm{coh.}}(\mathrm{Zr_2CuH}) = -0.255$ eV/atom. The stabilization along with the x_H content goes with increasing amounts of electrons which should mainly go into bonding states. This is addressed in the following section within the chemical bonding analysis. It is important to mention that the slight increase of energy with the 5th hydrogen is in agreement with the experimental observation that the H5 site is only partially occupied. Compared to other compound with the same stoichiometry, the cohesive energy of the saturated compound is close to the one computed for $\mathrm{Zr_2CoH_5}$ ($E_{\mathrm{coh.}} = -0.488$ eV/atom) lower than the more ionic $\mathrm{Mg_2CoH_5}$ with $E_{\mathrm{coh.}} = -0.343$ eV/atom [26].

Lastly a charge analysis for the different compositions of the monoclinic structure gives:

$\mathrm{Zr_2CuH}$: $Q(\mathrm{Zr}) = +1.13e$; $Q(\mathrm{Cu}) = -1.26e$; $Q(\mathrm{H1}) = -0.76e$.

$\mathrm{Zr_2CuH_2}$: $Q(\mathrm{Zr}) = +1.39e$; $Q(\mathrm{Cu}) = -1.22e$; $Q(\mathrm{H1}) = -0.74e$; $Q(\mathrm{H2}) = -0.78e$.

$\mathrm{Zr_2CuH_3}$: $Q(\mathrm{Zr}) = +1.50e$; $Q(\mathrm{Cu}) = -0.89e$; $Q(\mathrm{H1}) = -0.70e$; $Q(\mathrm{H2}) = -0.74e$; $Q(\mathrm{H3}) = -0.62e$.

$\mathrm{Zr_2CuH_4}$: $Q(\mathrm{Zr}) = +1.60e$; $Q(\mathrm{Cu}) = -0.57e$; $Q(\mathrm{H1}) = -0.69e$; $Q(\mathrm{H2}) = -0.70e$; $Q(\mathrm{H3}) = -0.59e$; $Q(\mathrm{H4}) = -0.60e$.

$\mathrm{Zr_2CuH_5}$: $Q(\mathrm{Zr}) = +1.67e$; $Q(\mathrm{Cu}) = -0.22e$; $Q(\mathrm{H1}) = -0.67e$; $Q(\mathrm{H2}) = -0.69e$; $Q(\mathrm{H3}) = -0.56e$; $Q(\mathrm{H4}) = -0.59e$; $Q(\mathrm{H5}) = -0.46e$.

These results allow suggesting a mechanism of charge transfers with increasing amounts of hydrogen: the Zr substructure becomes increasingly ionized through transferring electrons to the hydrogen sites; on the opposite Cu which is more electronegative is decreasingly ionized; especially from H3 to H4 and H5, where it starts contributing to the coordination polyhedron by sharing electrons partly with corresponding hydrogen. This can also be explained starting from fluorite structure $\mathrm{ZrH_2}$ for which the calculations show it as characterized by a relatively large cohesive energy: $E_{\mathrm{coh.}} = -0.614$ eV/atom and a large charge carried by hydrogen of $\sim -0.79e$. In $\mathrm{MgH_2}$ the hydrogen charge is $-0.83e$ [27]. Comparatively, the presently studied ternaries, all have cohesive energies below that of $\mathrm{ZrH_2}$ and the charges are less ionic. The iono-covalent character increases with copper as a whole, *i.e.* even before it comes in the environment polyhedron and then when it within [Zr_3Cu] tetahedron.

4.2. Energy–volume equations of states

Hydrogen insertion expands the host structure (cf. Table 1) and interacts with the metal substructures. The first effect which can be regarded as "negative pressure" increases interatomic metal–metal spacing and decreases the magnitude of the overlap between the orbital ensuring for the bonding. If the expansion role is prevailing then one expects a more compressible hydrogenated compound. The bonding magnitude effect is analyzed in Section 5 pertaining to the chemical bonding. The expansion effect can be examined through the equilibrium zero pressure parameters from the energy–volume, $E(V)$, equation of state (EOS) with calculations around minima found from geometry optimization. The resulting values are plotted in Fig. 3. The fit of the curves with 3rd order Birch EOS [28]:

$$E(V) = E_o(V_o) + [9/8]V_oB_o[([(V_o)/V])^{[2/3]} - 1]^2 + [9/16]B_o(B^{\wedge\prime} - 4)V_o[([(V_o)/V])^{[2/3]} - 1]^3,$$

provides E_o, V_o, B_o and B' respectively as the equilibrium energy, the volume, the bulk modulus and its pressure derivative. For tetragonal $\mathrm{Zr_2Cu}$ and $\mathrm{Zr_2CuH_2}$ and for monoclinic $\mathrm{Zr_2CuH_5}$, the $E(V)$ curves are given in Fig. 3 with the inserts showing the fit values.

The equilibrium energies and volumes show good agreement with geometry optimized values. B′ which is around 4 for all three compounds, is a magnitude unusually encountered (cf. [11]. and therein cited works). In spite of the volume increase from the intermetallic to the dihydride and then to the pentahydride, the bulk modulus B_0 increases continuously. This is a signature of the effects of hydrogen bonding with the metal substructure. Such an effect is found prevailing over the volume expansion.

5. Electronic density of states and chemical bonding properties

The calculated crystal parameters displayed in Table 1 were used in subsequent calculations of the electronic density of states and the chemical bonding assuming spin degeneracy for all species (non magnetic configuration). At self consistent convergence the charge transfer follows the trends observed above with less magnitude and additional charge residues (corresponding to less than 0.15 electrons) from the atomic spheres to IS.

Fig. 4(a) and (b) show the site projected density of states (PDOS) for tetragonal $\mathrm{Zr_2Cu}$ and $\mathrm{Zr_2CuH_2}$ respectively accounting for site multiplicities. Along the abscissa axis the energy is brought to the Fermi level E_F. As expected from the filling of the upper most shells, *i.e.* Zr ($5s^24d^2$) and Cu ($4s^13d^{10}$), the valence band (VB) is dominated by Cu ($3d$) saturated states centered and localized well below E_F at −4 eV. A visual inspection of the hydride's PDOS shows little changes for Cu upon hydrogen uptake. Higher intensity Zr PDOS peaks are seen at E_F for the hydride contrary to pristine binary due to the two H s-electrons injected within VB. The latter can be explained by the presence of H in [Zr_4] tetrahedra (Hypo. 1, ground state), whence a significant Zr–H bonding. The latter is further evidenced by the similar shape of H and Zr PDOS lines within [−5 eV; −10 eV]. However the larger PDOS due to Zr at E_F does not lead to magnetic instability as tested by trial spin polarized

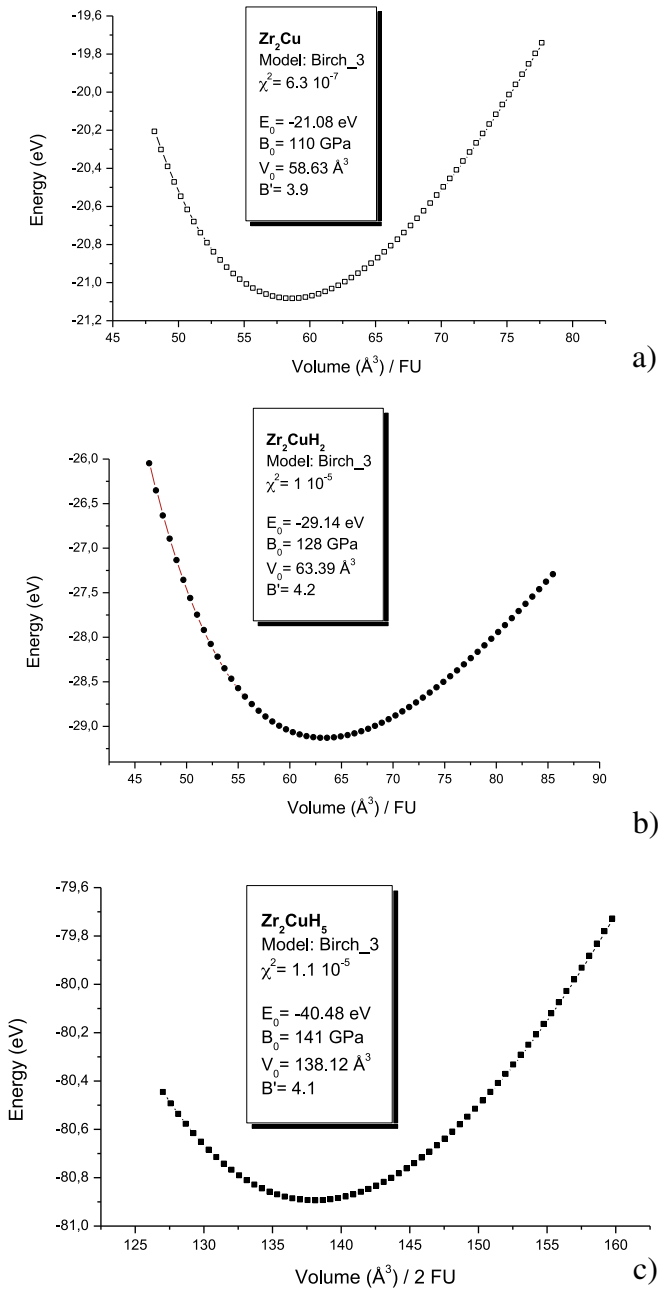

Fig. 3. Energy versus volume equations of states of: (a) body center tetragonal Zr_2Cu, (b) Zr_2CuH_2, and (c) body centered monoclinic Zr_2CuH_5. Respective fit values from Birch 3rd order EOS are given in inserts. χ^2 values indicate the goodness of fit.

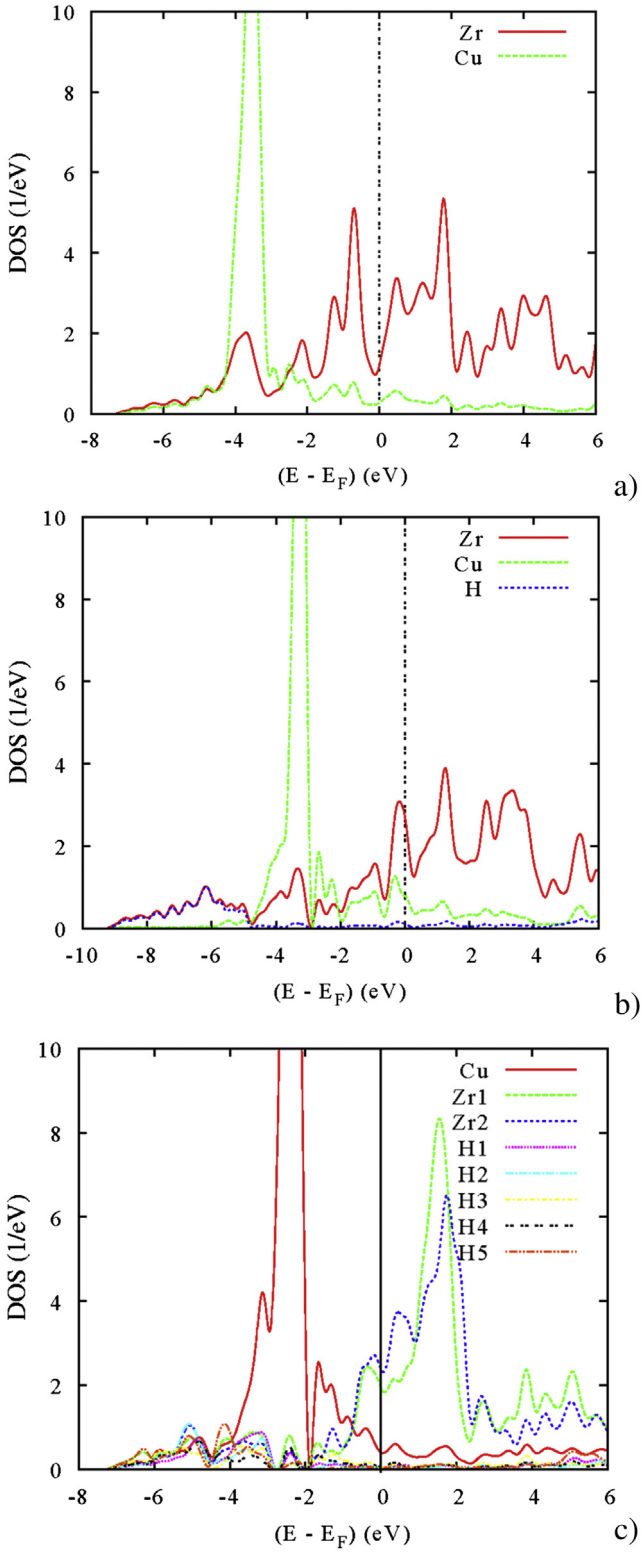

Fig. 4. Site projected PDOS for: (a) Zr_2Cu, (b) Zr_2CuH_2, and (c) Zr_2CuH_5.

calculations. A broader VB is observed for the hydride with respect to the intermetallic brought by H *s*-states.

PDOS for monoclinic Zr_2CuH_5 are depicted in Fig. 4(c). This saturated hydride exhibits similar PDOS features despite the presence of two Zr substructures but a broader and closer to E_F Cu *d*-states peak is observed at −3 eV. This can be explained by the presence of Cu within hydrogen surroundings (H3, H4, and H5) contrary to Zr_2CuH_2 where H is found in [*Zr*$_4$] tetrahedra.

Shedding light on the changes of interatomic species interactions upon H uptake is illustrated with chemical bonding analysis based on COOP criterion described above. This is shown in Fig. 5 for Zr_2Cu and its dihydride. Inter-metal interactions in pristine intermetallic (cf. Fig. 5(a)) are all of bonding nature throughout the VB, *i.e.* with positive intensities along the ordinate axis for most dominant Cu–Zr and Zr–Zr. Drastic changes occur upon H insertion, as shown in Fig. 5(b), with prevailing Zr–Cu bonding whereas Zr–Zr are vanishingly small. This is structurally relevant as Zr constitutes H surroundings in [*Zr4*]

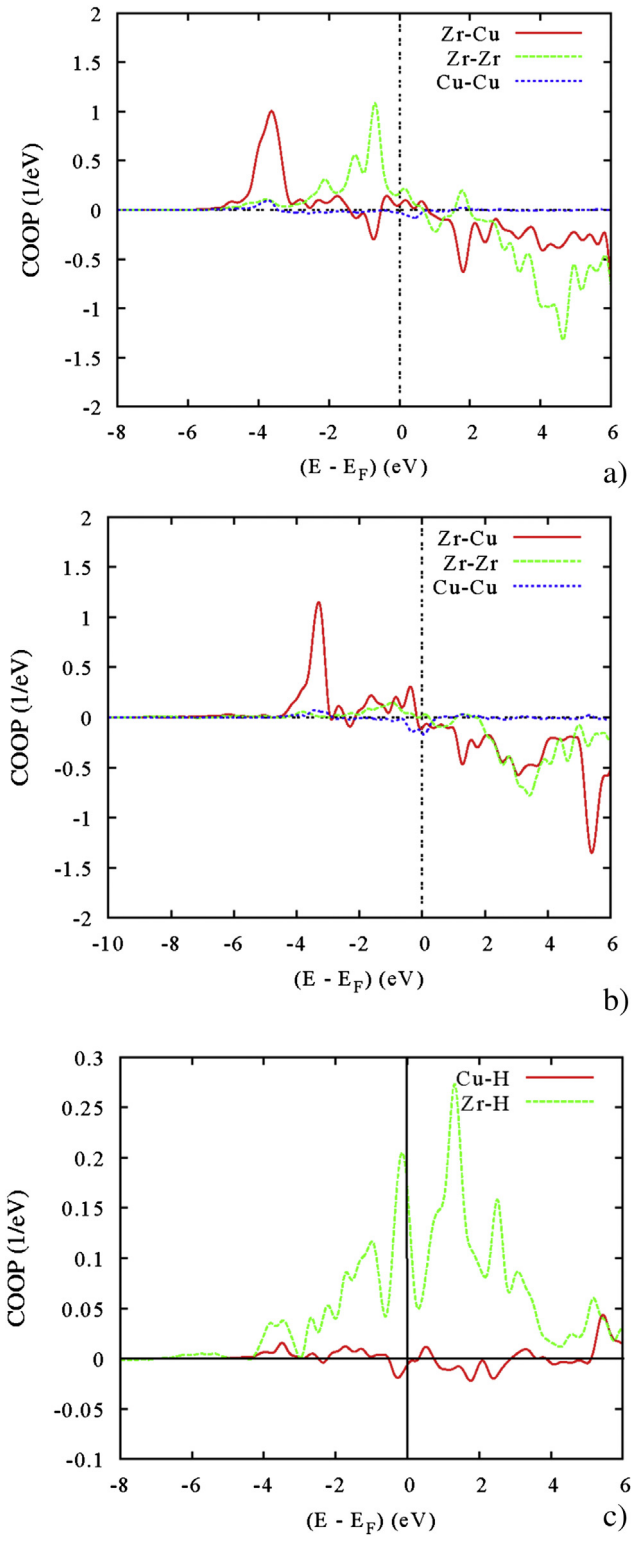

Fig. 5. COOP plots of: (a) metal–metal interactions in Zr_2Cu, (b) metal–metal interactions in Zr_2CuH_2, and (c) metal–H interactions in Zr_2CuH_2.

tetrahedra. Metal–H interactions are nicely reflected in Fig. 5(c) with prevailing Zr–H bonding throughout the VB. The overall metal–metal COOP in the dihydride are then weaker than in the intermetallic. The latter is concomitant with the cohesive energies on the one hand and the hindering brought by H on the other hand.

6. Conclusion

Crystal symmetry changes from tetragonal Zr_2CuH_2 to monoclinic Zr_2CuH_5 induced by H uptake are explained from cohesive energies computed for Zr_2CuH_x ($x = 1, 2, 3, 4, 5$) models. The structural crossover is identified at $2 < x < 3$ in agreement with experiment. For higher H composition, metal-to-metal interactions are weakened while metal–H bonding prevails leading to harder hydrides. Furthermore, Zr–H interactions are stronger than Cu–H. The latter suggests an H ordering in $[Zr_4]$ tetrahedra then $[Zr_3Cu_2]$ prisms within Zr_2CuH_5. From Bader charge analysis, H in $[Zr_3Cu_2]$ is found less ionic due to the presence of more electronegative Cu with respect to Zr leading to better kinetics for potential applications.

Acknowledgment

We acknowledge financial support from French-Lebanese CEDRE project and CSR-USEK. Part of the calculations where done on MCIA super computers of the University Bordeaux 1. We thank Conseil Regional d'Aquitaine for support. We acknowledge technical help with documentation from Mrs Catherine MARC of the Science Library of the Université Bordeaux 1.

References

[1] Wallace WE, Epstein LM. J Chem Phys 1961;35:2238.
[2] Bailey DM, Smith JF. Acta Cryst 1961;14:1084.
[3] Kobayashi E, Matsumoto S, Doi H, Yoneyama T, Hamanaka H. J Biomed Mater Res 1995;29:943.
[4] Semenova EL, Kudryavtsev YV. J Alloys Compd 1994;203:165.
[5] Wiesinger G, Paul-Boncour V, Filipek SM, Reichl Ch, Marchuk I, Percheron-Guégan A. J Phys Condens Matter 2005;17:893.
[6] Kirkpatrick ME, Bailey DM, Smith JF. Acta Cryst 1962;115:252.
[7] Jensen IJT. Structural studies of hydrides of Zr_2Cu, Zr_2Pd and LaPtIn. (Thesis). Norway: University of Oslo.
[8] Maeland AJ, Libowitz GG. J Less Common Met 1980;74:295–300.
[9] Paul-Boncour V, Matar SF. Phys Rev B 2004;70:184435.
[10] Matar SF. Prog Solid State Chem 2010;38:1–37.
[11] Matar SF. Intermetallics 2013;36:25.
[12] Hohenberg P, Kohn W. Phys Rev B 1964;136:864;
Kohn W, Sham LJ. Phys Rev A 1965;140:1133.
[13] Kohlmann H, Kurtzemann N, Weihrich R, Hansen T, Anorg Z. Allg Chem 2009;635:2399.
[14] Herbst JF, Hector Jr LG. Appl Phys Lett 2004;85:3465.
[15] Kresse G, Furthmüller J. Phys Rev B 1996;54:11169;
Kresse G, Joubert J. Phys Rev B 1999;59:1758.
[16] Blöchl PE. Phys Rev B 1994;50:17953.
[17] Perdew J, Burke K, Ernzerhof M. Phys Rev Lett 1996;77:3865.
[18] Ceperley DM, Alder BJ. Phys Rev Lett 1980;45:566.
[19] Press WH, Flannery BP, Teukolsky SA, Vetterling WT. Numerical recipes. New York: Cambridge University Press; 1986.
[20] Methfessel M, Paxton AT. Phys Rev B 1989;40:3616.
[21] Williams AR, Kübler J, Gelatt CD. Phys Rev B 1979;19:6094.
[22] Eyert V. The augmented spherical wave method – a comprehensive treatmentIn Lecture notes in physics. 2nd ed., vol. 849. Heidelberg: Springer; 2013.
[23] Hoffmann R. Angew Chem Int Ed Engl 1987;26:846.
[24] Bader R. Chem Rev 1991;91:893.
[25] Tang W, Sanville E, Henkelman G. J Phys Condens Matter 2009;21:084204. http://theory.cm.utexas.edu/henkelman/research/bader.
[26] Matar SF. J Solid State Chem 2013;200:209.
[27] Vajeeston P, Ravindran P, Fjellvåg H. Nanotechnology 2008;19:275704.
[28] Birch F. J Geophys Res 1978;83:1257.